Article:
Yang, F., Hu, Y., Hu, Q. et al. (2022) Electrical and dielectric properties of Ca-doped bi-deficient sodium bismuth titanate Na0.5Bi0.49−xCaxTiO3−δ (0 ≤ x ≤ 0.08). Crystals, 12 (12). 1800. ISSN: 2073-4352

https://doi.org/10.3390/cryst12121800

crystals

MDPI

Article

Electrical and Dielectric Properties of Ca-Doped Bi-Deficient Sodium Bismuth Titanate $Na_{0.5}Bi_{0.49-x}Ca_xTiO_{3-\delta}$ ($0 \leq x \leq 0.08$)

Fan Yang [1,*], Yidong Hu [2], Qiaodan Hu [2], Patrick Wu [3] and Derek C. Sinclair [3]

[1] Institute of Fuel Cells, School of Mechanical Engineering, Shanghai Jiao Tong University, Shanghai 200240, China
[2] School of Materials Science and Engineering, Shanghai Jiao Tong University, Shanghai 200240, China
[3] Department of Materials Science & Engineering, University of Sheffield, Sheffield S1 3JD, UK
* Correspondence: fanyang_0123@sjtu.edu.cn

Abstract: Bismuth-deficient sodium bismuth titanate (nominal $Na_{0.5}Bi_{0.49}TiO_{2.985}$, $NB_{0.49}T$) presents high oxide ion conductivity, which makes it a potential electrolyte material for intermediate-temperature solid oxide fuel cells. Acceptor doping has been proven an effective approach to enhance the bulk conductivity (σ_b) of $NB_{0.49}T$. Here, divalent Ca^{2+} ions were selected to partially replace Bi^{3+} on the A-site of $NB_{0.49}T$, and the temperature and composition dependences of σ_b and permittivity were investigated. Results showed that Ca^{2+} doping was effective for enhancing σ_b of $NB_{0.49}T$ by creating oxygen vacancies. The highest σ_b (0.006 S·cm^{-1} at 500 °C) was achieved by 2% Ca^{2+} doping. Further increase in the doping level decreased σ_b, which was more pronounced at temperatures below ~350 °C. Most importantly, Ca doping increased the temperature at which the activation energy for bulk conduction changed from ~0.80 eV (at low temperatures) to ~0.40 eV (at high temperatures), and reduced the temperature dependence of permittivity of $NB_{0.49}T$. Results from the average structural parameters and the local defect associates are discussed. The findings of this work are helpful for understanding the defect and conduction mechanisms for acceptor-doped $NB_{0.49}T$, and are also useful for developing NBT-based dielectrics with temperature -independent permittivity.

Keywords: sodium bismuth titanate; acceptor doping; oxide ion conductivity; impedance spectroscopy; permittivity

Citation: Yang, F.; Hu, Y.; Hu, Q.; Wu, P.; Sinclair, D.C. Electrical and Dielectric Properties of Ca-Doped Bi-Deficient Sodium Bismuth Titanate $Na_{0.5}Bi_{0.49-x}Ca_xTiO_{3-\delta}$ ($0 \leq x \leq 0.08$). *Crystals* **2022**, *12*, 1800. https://doi.org/10.3390/cryst12121800

Academic Editor: Pavel Lukáč

Received: 6 November 2022
Accepted: 5 December 2022
Published: 10 December 2022

1. Introduction

Development of intermediate-temperature solid oxide fuel cells (IT-SOFCs) raises urgent demand for novel electrolyte materials with higher oxide ion conductivity than the state-of-the-art yttria-stabilized zirconia (YSZ). In 2014, a new family of oxide ion conductors based on the ferroelectric perovskite sodium bismuth titanate ($Na_{0.5}Bi_{0.5}TiO_3$, NBT) was reported [1]. Since then, numerous efforts have been devoted to enhancing the bulk conductivity (σ_b) of NBT by introducing A-site cation nonstoichiometry and/or acceptor doping [2–21], based on which the following cognitions have been established: (1) high oxide-ion conductivity can be obtained in Na-rich or Bi-deficient NBT, e.g., $Na_{0.51}Bi_{0.5}TiO_{3.005}$ ($N_{0.51}BT$) or $Na_{0.5}Bi_{0.49}TiO_{2.985}$ ($NB_{0.49}T$) [2]; (2) acceptor doping, either on A-site (e.g., partial replacement of Bi^{3+} by Sr^{2+} [3]) or B-site (e.g., partial substitution of Ti^{4+} by Mg^{2+} [1]), generates oxygen vacancies by an ionic compensation mechanism, and therefore is an effective approach for enhancing the σ_b of NBT [8]; (3) σ_b of acceptor-doped $NB_{0.49}T$ is higher than that of yttria-stabilized zirconia (YSZ) at < 600 °C, and it shows no appreciable degradation at 500 °C contrary to the rapid conductivity decay for rare-earth- stabilized δ -Bi_2O_3 [6], which makes NBT-based oxide ion conductors promising candidate electrolyte materials for IT-SOFCs.

Among all the acceptor-type dopants, Mg^{2+} is the most widely investigated B-site dopant for NBT. The initial work by Li et al. [1] employed Mg^{2+} to replace Ti^{4+} in $NB_{0.49}T$,

and reported an enhancement of σ_b by ~half order of magnitude by 2% Mg doping. Further enhancement of σ_b by increasing the doping level was proven undesirable due to the low solubility of Mg^{2+} in $NB_{0.49}T$, i.e., a Ti-rich secondary phase was observed in 2% Mg-doped $NB_{0.49}T$. Later work by Singh et al. [11] reported a similar effect, that the highest conductivity can be obtained in 2% Mg-doped $NB_{0.49}T$ prepared by a polyol-mediated synthesis route. Bhattacharyya et al. [12] incorporated Mg^{2+} to highly nonstoichiometric $Na_{0.54}Bi_{0.46}TiO_{3-\delta}$ and obtained the highest σ_b by 1% Mg doping. The phenomenon that there exists an optimum doping level, above which σ_b decreases with increasing doping level, has been widely observed in NBT with other B-site dopants such as Ga^{3+}, Al^{3+}, Sc^{3+}, and Fe^{3+} [8–10,15,16]. The limited enhancement of σ_b by B-site acceptor doping was first explained by He and Mo by first-principles calculations [22]. Their results showed that acceptor doping on the B-site could significantly increase the oxygen migration barriers by binding with oxygen vacancies, which suppresses the mobility of oxygen ions and therefore is detrimental to oxide ion conduction. Formation of defect association between the positively charged acceptor dopants and the negatively charged oxygen vacancies, as well as its effect on the σ_b of NBT, was further revealed by researchers [14,23,24], and it has been widely adopted to explain the variation of σ_b with doping level.

Based on the first-principles calculations [22], a novel doping strategy on the A-site was proposed as a more beneficial approach to enhance the σ_b of NBT because the disordered A-site sublattice can form different local atomistic configurations to accommodate the electrostatic and strain fields of the dopant ions. It was predicted that partial replacement of Bi^{3+} by monovalent Na^+ or K^+, e.g., $Na_{0.54}Bi_{0.46}TiO_{2.96}$ or $Na_{0.5}K_{0.04}Bi_{0.46}TiO_{2.96}$, could induce higher σ_b than Mg doping given the same oxygen vacancy concentration. Inspired by the above theoretical prediction, acceptor-type dopants such as Li^+, Na^+, K^+, Ca^{2+}, Sr^{2+}, and Ba^{2+} were selected to partially replace Bi^{3+} on the A-site of NBT. For example, Shih et al. [17,18] prepared Li- and K-doped $NB_{0.50}T$ by a modified Pechini citrate–nitrate synthesis route and achieved an enhancement of the total conductivity by ~ one order of magnitude by 4% Li or K doping. However, the highest conductivity reached by 4% Li doping was still lower than that of 2% Mg-doped NBT, which disagrees with the theoretical prediction that acceptor doping on the A-site is superior to that on the B-site. Bhattacharyya et al. [12] prepared $Na_{0.54}Bi_{0.46}TiO_{2.96}$ (4% Na-doped $NB_{0.50}T$) ceramics but Na, Ti-rich secondary phases were observed under SEM. Moreover, Li, Na, or K doping can be experimentally unfavorable because of the high volatility of these elements, which makes it difficult to control the composition of sintered ceramics.

Non-volatile elements from the IIA family, M = Ca, Sr, and Ba, were therefore considered as more promising dopants to replace Bi^{3+} on the A-site of NBT. Previously, we prepared 2% M^{2+}-doped $NB_{0.49}T$ ceramics and investigated their electrical properties [7]. The preliminary results suggest these divalent dopants are all effective to enhance the σ_b of $NB_{0.49}T$ without changing the conduction mechanism, and Ca^{2+} and Sr^{2+} are more effective in enhancing σ_b than Ba^{2+}. We discussed the dependence of σ_b on the type of dopant ions from the variation of average structural parameters (tolerance factor and specific free volume) induced by doping, as well as the intrinsic properties of dopant ions including ionic radius, polarizability, and bonding strength with oxygen. We proposed that, at low doping levels (thus the change of average structural parameters induced by doping is negligible), a small mismatch in the ionic radius between M^{2+} and Bi^{3+}, a large polarizability and a low M–O bonding energy are beneficial for obtaining high σ_b. Although we casted doubt on any significant enhancement of σ_b by increasing the doping level because (1) the gain from an increase in the oxygen vacancy concentration may be offset by lower polarizability and higher M–O bonding strength of the dopant; (2) Na,Ti-rich secondary phases were observed in 2% M^{2+}-doped $NB_{0.49}T$ (sintered at 1150 °C) under SEM; and (3) a physical upper limit of σ_b calculated from the oxygen vacancy diffusivity limit model in the perovskite lattice suggested optimization of σ_b may have been achieved [8]; experimental evidence is still required to verify this conjecture.

Here we have selected divalent Ca^{2+} ions to partially replace Bi^{3+} on the A-site of $NB_{0.49}T$, and prepared a series of Ca-doped $NB_{0.49}T$ ceramics with the doping level varying from 2% to 8% by the conventional solid state reaction method. The composition and temperature dependencies of σ_b and permittivity of these ceramics were investigated primarily by impedance spectroscopy. Ca was selected for investigation due to the following reasons: (1) $CaTiO_3$ is well known to form a solid solution with NBT with a large solubility [25,26]. It is possible that, if sintered under proper temperatures, the solubility of Ca^{2+} in NBT may be potentially high to create a high level of oxygen vacancies to facilitate charge carriers; and (2) Ca^{2+} has a smaller ionic radius than Bi^{3+} [7], therefore, substitution of Bi^{3+} by Ca^{2+} will decrease the tolerance factor (t) of $NB_{0.49}T$ from ~0.98 towards the optimum value of ~0.96 for maximum conductivity in perovskites [27]. Results show dense and clean (by XRD) Ca-doped $NB_{0.49}T$ ceramics can be obtained when sintered at 1100 °C. Unexpectedly but interestingly, we found Ca doping could increase the temperature at which the activation energy for bulk conduction changes from ~0.80 eV (at low temperatures) to ~0.40 eV (at high temperatures), which has not been reported in other acceptor-doped NBT ceramics. Ca doping also decreases the temperature dependence of permittivity of $NB_{0.49}T$. Findings of this work are not only helpful for designing NBT-based oxide ion conductors by acceptor doping, but also useful for developing NBT-based dielectrics with temperature-independent permittivity.

2. Experimental

Ca-doped $NB_{0.49}T$ ceramics with nominal compositions of $Na_{0.5}Bi_{0.49-x}Ca_xTiO_{3-\delta}$ ($0.02 \leq x \leq 0.08$) were prepared by solid-state reaction using Na_2CO_3 (99.5%, Fisher chemical, Loughborough, UK), Bi_2O_3 (99.9%, Acros Organics, Pittsburgh, USA), TiO_2 (99.9%, Sigma Aldrich, Dorset, UK) and $CaCO_3$ (99.0%, Sigma Aldrich, Dorset, UK) as starting materials. The above raw materials were dried overnight at 300 °C for Bi_2O_3 and Na_2CO_3, 180 °C for $CaCO_3$, and 800 °C for TiO_2. Appropriate amounts of each precursor were weighed and mixed thoroughly in isopropanol using yttria-stabilized zirconia grinding media for 6 h using a laboratory roller-ball milling machine. Subsequently, the mixture was transferred to a beaker, dried at 85 °C overnight, sieved, and calcined at 800 °C for 2 h. The resultant powders were subjected to a second round of ball milling (4 h), drying, sieving, and calcination, and finalized by a third round of ball milling (6 h), drying, and sieving. The final products were compacted into pellets by uni-axial cold pressing followed by isostatic pressing at 200 MPa. Pellets were embedded in sacrificial powder of the same composition to reduce sodium and/or bismuth loss at high temperature, and sintered at 1100 °C for 2 h. Undoped $NB_{0.49}T$ was prepared by identical procedures but sintered at 1150 °C for 2 h to obtain dense ceramics.

Phase purity was identified by X-ray diffraction on the crushed pellets using a high-resolution STOE STADI-P diffractometer (STOE & Cie GmbH, Darmstadt, Germany) operating with $CuK\alpha_1$ radiation with a linear position-sensitive detector. The crushed pellets were annealed at 400 °C for 4 h to eliminate any residual stress caused by crushing and grinding. Lattice parameters were determined by structural refinement for reflections in the range of $10° \leq 2\theta \leq 100°$ using the Rietveld refinement program GSAS with the EXPGUI interface [28,29]. Ceramic microstructure was observed by scanning electron microscopy on thermally etched surfaces using a Philips XL 30 SEM. Compositions were examined by energy dispersive X-ray spectroscopy (EDS) on carbon-coated, polished, and thermally-etched surfaces.

Electrical properties of the pellets were obtained via AC impedance spectroscopy using an Agilent E4980A impedance analyzer (Agilent Technologies Inc., Palo-Alto, CA, USA). Before measurement, Au paste was coated onto the polished surfaces of the samples and fired at 800 °C for 2 h to serve as electrodes. For impedance measurements, an alternating voltage of 0.1 V was applied to the sample over a frequency range from 1 MHz to 2 Hz at different temperatures. Impedance measurements were also carried out in flowing nitrogen, air, and oxygen using a Solartron 1260 system (Solartron Analytical, Leicester,

UK; frequency range of 1 MHz to 0.1 Hz). Equivalent circuit fittings of the impedance data were analyzed using Zview Impedance Analysis software (Scribner Associates, Inc., Southern Pines, North Carolina, USA). All impedance data were corrected for high-frequency inductance by performing a short-circuit measurement and normalized by a geometric factor $\alpha = \frac{4t}{\pi D^2}$, where t and D denote the thickness and the diameter of the pellet, respectively. The resistance and the capacitance data were reported in units of Ω·cm and $F \cdot cm^{-1}$, respectively.

3. Results

3.1. Crystal Structure, Microstructure, and Composition

The sintered $Na_{0.5}Bi_{0.49-x}Ca_xTiO_{3-\delta}$ ceramics were phase-pure, based on laboratory XRD (Figure 1a). The main peak at 2θ~32.5° shows a systematic shift to higher angle with increasing x (Figure 1b), suggesting Ca^{2+} was successfully incorporated into the NBT lattice. A small superlattice reflection at 2θ~38.5° from the rhombohedral structure, as indicated by the dashed box in Figure 1c, can be observed for all compositions. Intensity of the superlattice peak decreased with increasing x. The crystal structure could be refined to a rhombohedral cell (space group $R3c$, Figure 1d, $x = 0.04$ as an example). The cell volume decreased with increasing x (Figure 1e) due to the smaller ionic radius of Ca^{2+} (1.34 Å [30]) than that of Bi^{3+} (~1.39 Å [31]) in 12-fold coordination. Lattice parameters and the fitting qualities are listed in Table 1.

Table 1. Lattice parameters and Rietveld fitting qualities of the $Na_{0.5}Bi_{0.49-x}Ca_xTiO_{3-\delta}$ ceramics.

x	Space Group	Lattice Parameters			Fitting Qualities	
		a (Å)	b (Å)	V (Å^3)	w_{Rp} (%)	χ^2
0	R3c	5.4901	13.5137	352.75	9.83	2.14
0.02	R3c	5.4903	13.4890	352.13	6.15	1.59
0.04	R3c	5.4957	13.4425	351.61	7.61	1.31
0.06	R3c	5.4931	13.4416	351.25	9.01	1.59
0.08	R3c	5.4902	13.4280	350.52	9.78	2.17

SEM micrographs of thermally-etched surfaces of the sintered $Na_{0.5}Bi_{0.49-x}Ca_xTiO_{3-\delta}$ ceramics are presented in Figure 2, where well-densified microstructure can be observed for all samples. The undoped $NB_{0.49}T$ has an average grain size, d~7.2 μm, which is larger than that of the Ca-doped $NB_{0.49}T$ ceramics due to the higher sintering temperature (1150 °C versus 1100 °C). The value of d decreases with increasing x from ~2.1 μm for $x = 0.02$ to ~1.6 μm for $x = 0.08$. EDS analysis shows that the atomic fractions of the A-site (Na, Bi, and Ca), and B-site (Ti) cations are close to their nominal values (Figure 3), which further confirms the successful incorporation of Ca^{2+} into $NB_{0.49}T$.

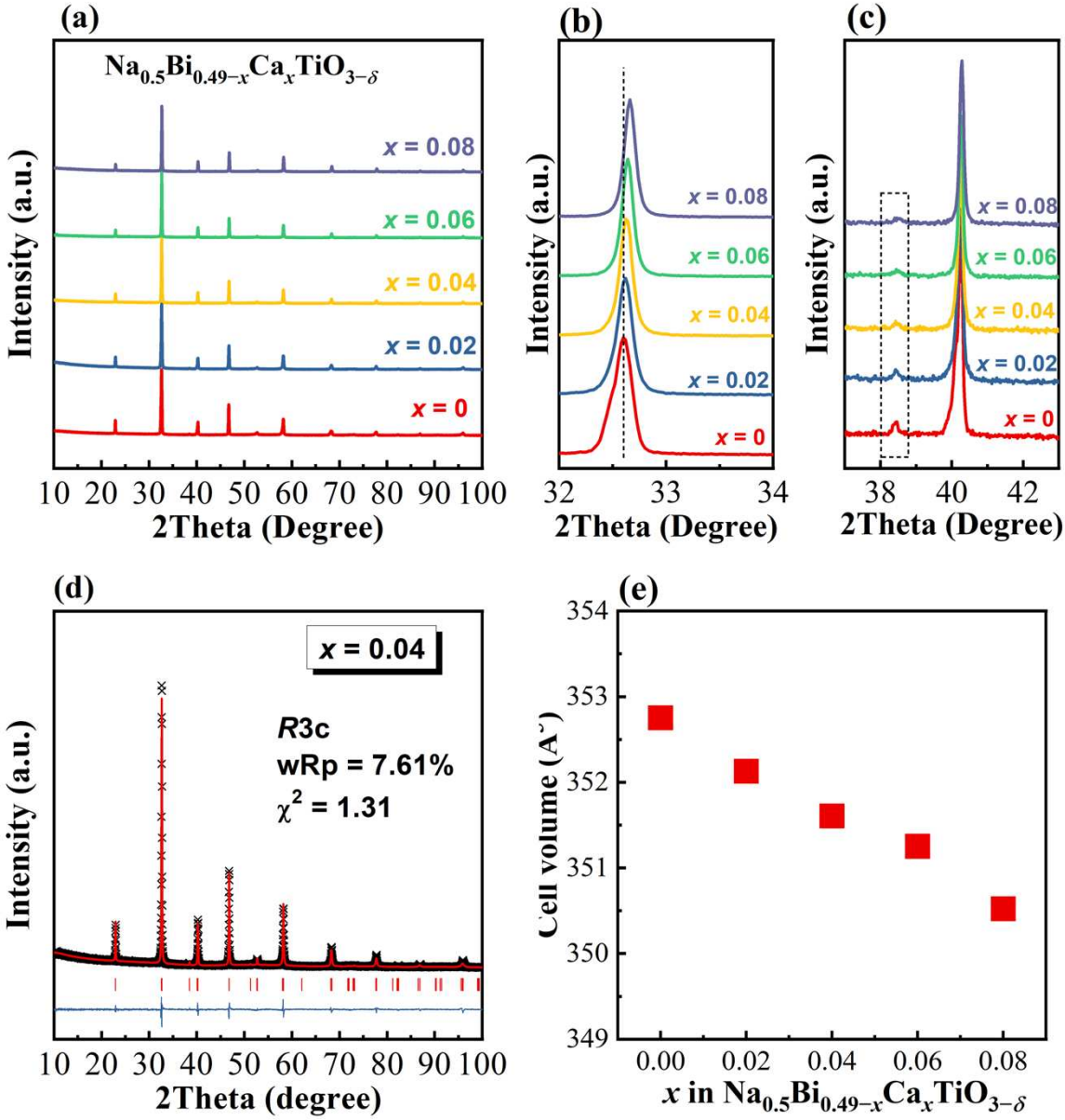

Figure 1. (**a**) XRD patterns of the $Na_{0.5}Bi_{0.49-x}Ca_xTiO_{3-\delta}$ ceramics; (**b**,**c**) expanded views of the 2θ range of 32–34° and 37–43°, respectively. The dashed vertical line in (**b**) shows the peak position for $x = 0$, and the dashed box in (**c**) indicates the superlattice peak from the rhombohedral structure. (**d**) Rietveld refinement of the XRD pattern ($x = 0.04$ as an example). Crosses represent the observed pattern and the solid line through the symbols shows the calculated fit. The reflection marker for the *R*3c structure of NBT is shown as vertical lines with the difference pattern below. The quality of fit is indicated in the figure. (**e**) Cell volume as a function of x.

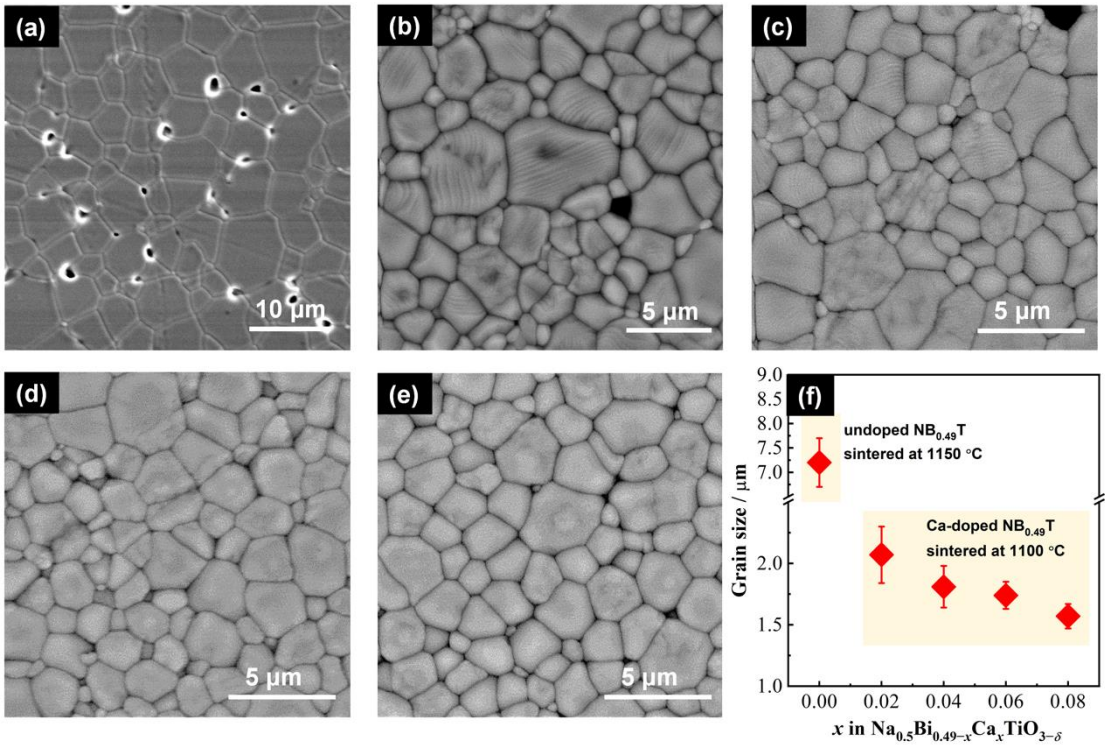

Figure 2. (**a**–**e**) SEM micrographs of the thermally etched surfaces of $Na_{0.5}Bi_{0.49-x}Ca_xTiO_{3-\delta}$: (**a**) $x = 0$; (**b**) $x = 0.02$; (**c**) $x = 0.04$; (**d**) $x = 0.06$; and (**e**) $x = 0.08$. (**f**) Average grain size as a function of x.

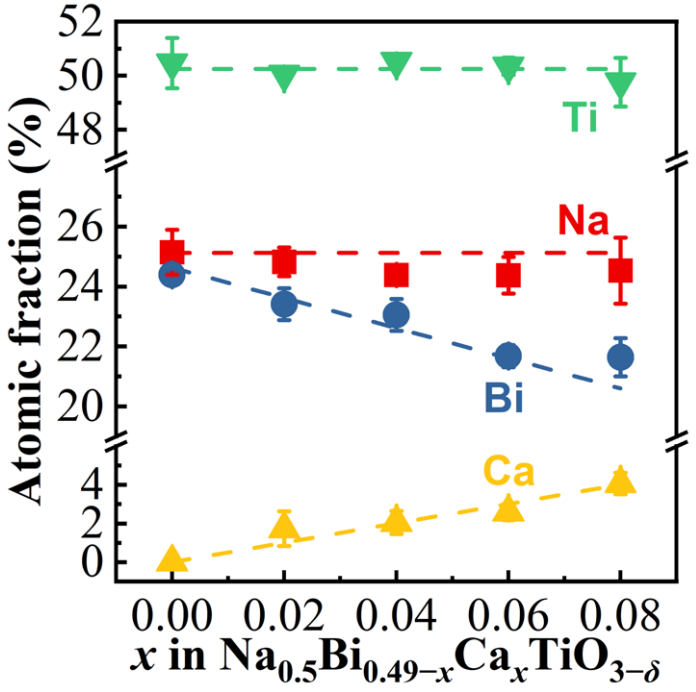

Figure 3. Atomic fraction of each cation in $Na_{0.5}Bi_{0.49-x}Ca_xTiO_{3-\delta}$ obtained from EDS. Data were collected from 5 randomly selected areas on polished surfaces (without thermal etching). The dashed lines indicate the nominal values.

3.2. Impedance Spectra

Impedance spectra of all the $Na_{0.5}Bi_{0.49-x}Ca_xTiO_{3-\delta}$ ceramics present typical features for oxide-ion-conducting NBT. To avoid unnecessary duplication, the impedance spectra for a selected composition, $x = 0.04$, are presented here. As displayed in Figure 4a, the complex plane Z^* plot at 300 °C shows three well-resolved arcs, and can be fitted by an equivalent circuit of three resistor-constant phase elements (*R*-*CPE*) connected in series (inset figure in Figure 4a). Apart from the Z^* plot, the impedance data and the associated fitting results are also presented in different formats (Figure 4b,c). As shown in Figure 4b, a single peak at ~550 kHz can be observed from the M''-log$f$ plot. The capacitance calculated from the M'' peak maximum according to $C = 0.5/M''_{max}$ is 1.38×10^{-10} F·cm^{-1}, corresponding to a relative permittivity of ~1570, which is consistent with the reported permittivity magnitude of ferroelectric NBT. Moreover, an expanded view of the high-frequency region of the $-Z''$-log$f$ plot (inset figure in Figure 4b) shows a peak at ~500 kHz. The very close high-frequency peak positions from M''-log$f$ and $-Z''$-log$f$ plots, along with the magnitude of the relative permittivity, confirm that the high-frequency response represents the bulk (grains) response. The C'-log$f$ plot (Figure 4c) shows two plateaus. The one with $C' \sim 1 \times 10^{-10}$ F·cm^{-1} at frequencies > 500 kHz agrees with the capacitance value calculated from the M''_{max}, and therefore represents the bulk response. The second plateau, with $C' \sim 3 \times 10^{-9}$ F·cm^{-1} in the frequency range between 10^3–10^4 Hz, suggests the response is from grain boundaries (GBs) [32]. In the lower frequency range < 10^3 Hz, C' increases with decreasing frequency and approaches 10^{-7} F·cm^{-1} at 20 Hz, indicating the low-frequency response originates from the electrode effect [32]. Combining the above information, it can be confirmed that the three arcs on the Z^* plot, from high to low frequency, correspond to the responses from the bulk, GBs, and electrode effect, respectively. In all formats, the fitted impedance curves agree well with the experimental data, and the impedance residuals, defined as $Z_{residuals} = (Z_{measured} - Z_{fitted})/|Z_{measured}|$ [33], are within 2% in the entire frequency range (Figure 4d). Agreements between the experimental and the fitted data, along with the low-impedance residuals, indicate the validity of the selected equivalent circuit and provide confidence in the extracted resistance and capacitance values.

At high temperatures, for example, 500 °C, the Z^* plot displays different features compared to that at lower temperatures. As shown in Figure 5a, from high to low frequency, the Z^* plot is featured by an intercept on the Z' axis, a small arc, and a highly distorted large tail, respectively. The impedance spectra, along with the fitting curves, are also presented in Bode plots (Figure 5b,c). As shown in Figure 5b, at frequencies > 10^4 Hz, M'' increased continuously with increasing frequency, indicating the M'' peak from the bulk response should appear at f > 1 MHz. On the other hand, a peak at ~10 kHz is presented on the $-Z''$-log$f$ plot; however, no peak is observed on the M''-log$f$ plot near this frequency, suggesting the response was associated with a large capacitance. In addition, the C'-log$f$ plot in Figure 5c, shows one plateau of ~10^{-9} F·cm^{-1} in the frequency range of 20–200 kHz. At lower frequencies (< 10^4 Hz), C' approaches 10^{-6} F·cm^{-1} at 20 Hz, indicating the low-frequency response originates from the electrode effect. Combining the above information, it can be concluded that the intercept on the Z' axis, the arc, and the large tail represent the responses from the bulk, the GBs, and the electrode effect, respectively. Therefore, an equivalent circuit, as presented in the top inset figure in Figure 5a, was selected to fit the impedance data, in which *L*1 and *R*1 represent the high-frequency induction from the equipment/wire connection and the intercept on the Z' axis, respectively; *R*2-*CPE*2 represents the intermediate-frequency response; *R*3, *W*1, and *CPE*3 are the parameters describing the charge transfer resistance, Warburg impedance, and the double-layer capacitance associated with the electrode process [34]. The impedance residuals were within 0.5% (Figure 5d), showing a high-fitting quality and providing confidence in the validity of the equivalent circuit and its associated fitting results.

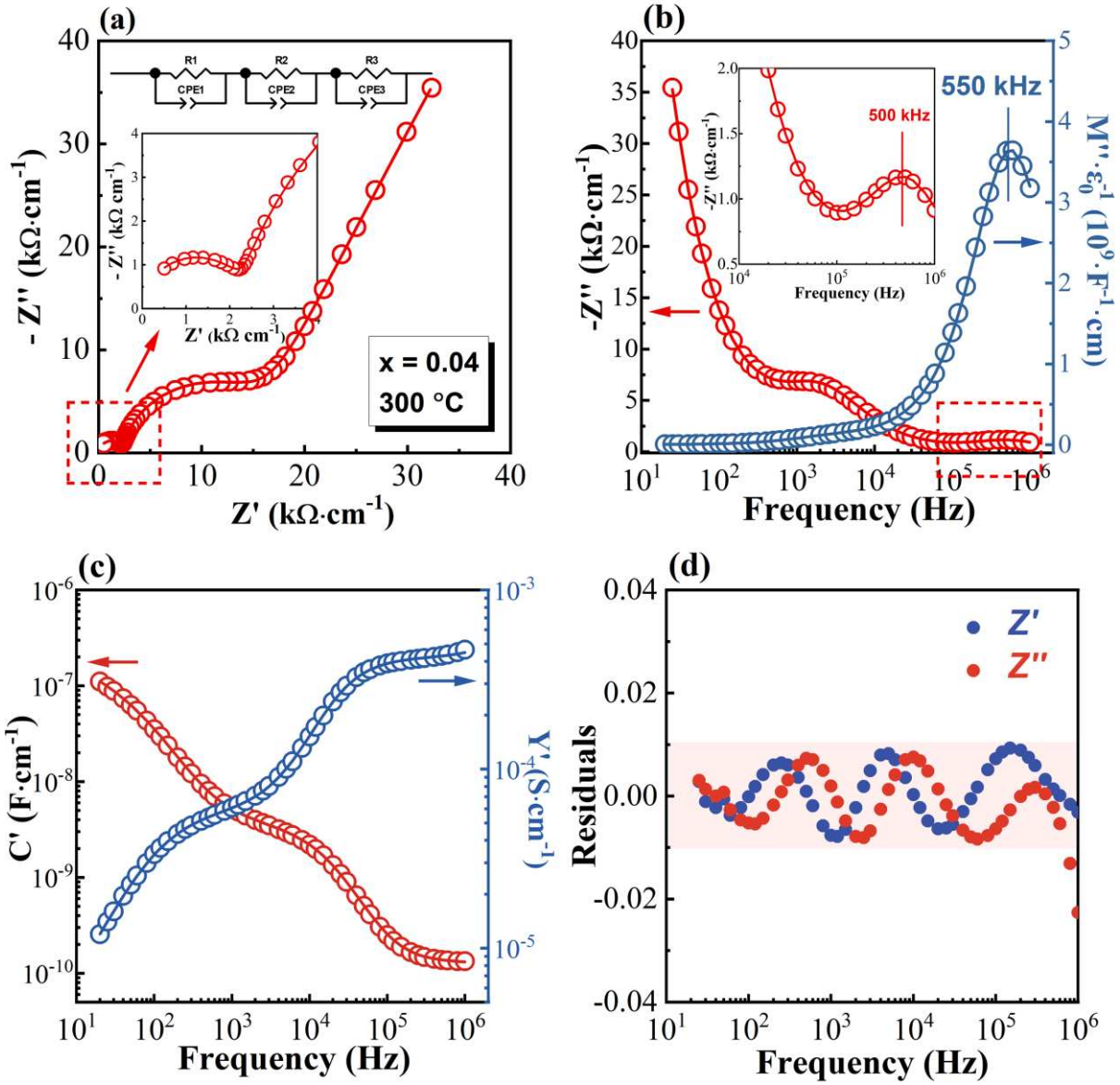

Figure 4. Impedance spectroscopy data and equivalent circuit-fitting results presented in different formats for a selected composition, x = 0.04, at 300 °C. (**a**) Z^* plot and the equivalent circuit used for fitting; (**b**) $-Z''$-log$f$ and M''-log$f$ plots; (**c**) C'-log$f$ and Y'-log$f$ plots; (**d**) Impedance residuals showing the quality of fit. In (**a**–**c**), the open circles are the experimental data and the solid lines across the symbols are the fitting curve. The inset figures in (**a**,**b**) are the expanded views of the high-frequency arc, as indicated by the dashed rectangles.

From the above equivalent circuit fittings, the bulk resistance (R_b) in the temperature range of 200–500 °C can be obtained, and subsequently converted to σ_b by $\sigma_b = 1/R_b$. Arrhenius plots for σ_b of $Na_{0.5}Bi_{0.49-x}Ca_xTiO_{3-\delta}$ ceramics and the compositional dependence of σ_b at selected temperatures are displayed in Figure 6a,b, respectively, from which the following information can be extracted: (1) σ_b values for Ca-doped $NB_{0.49}T$ ceramics were higher than that of $NB_{0.49}T$, confirming the effectiveness of enhancing σ_b by replacing Bi^{3+} by Ca^{2+} on the A-site of NBT; (2) the highest σ_b was achieved in 2% Ca-doped $NB_{0.49}T$, with an enhancement of σ_b by ~1 order of magnitude at temperatures > 350 °C, and ~0.5 order of magnitude at temperatures < 350 °C; (3) σ_b decreased with further increase in the Ca-doping level, which was more pronounced at temperatures below 350 °C. At temperatures > 400 °C, σ_b values for Ca-doped $NB_{0.49}T$ showed very small variation with the doping level; (4) for all compositions, a change in the activation energy (E_a) could be observed

within the temperature range investigated. The temperature where E_a changed (T_{Ea}) was dependent on the Ca-doping level. As shown in Figure 6c, T_{Ea} increased with increasing x from ~325 °C for x = 0 to > 400 °C for x = 0.08. E_a varied between 0.75 and 0.84 eV at temperatures below T_{Ea}, and between 0.37 and 0.43 eV above T_{Ea}.

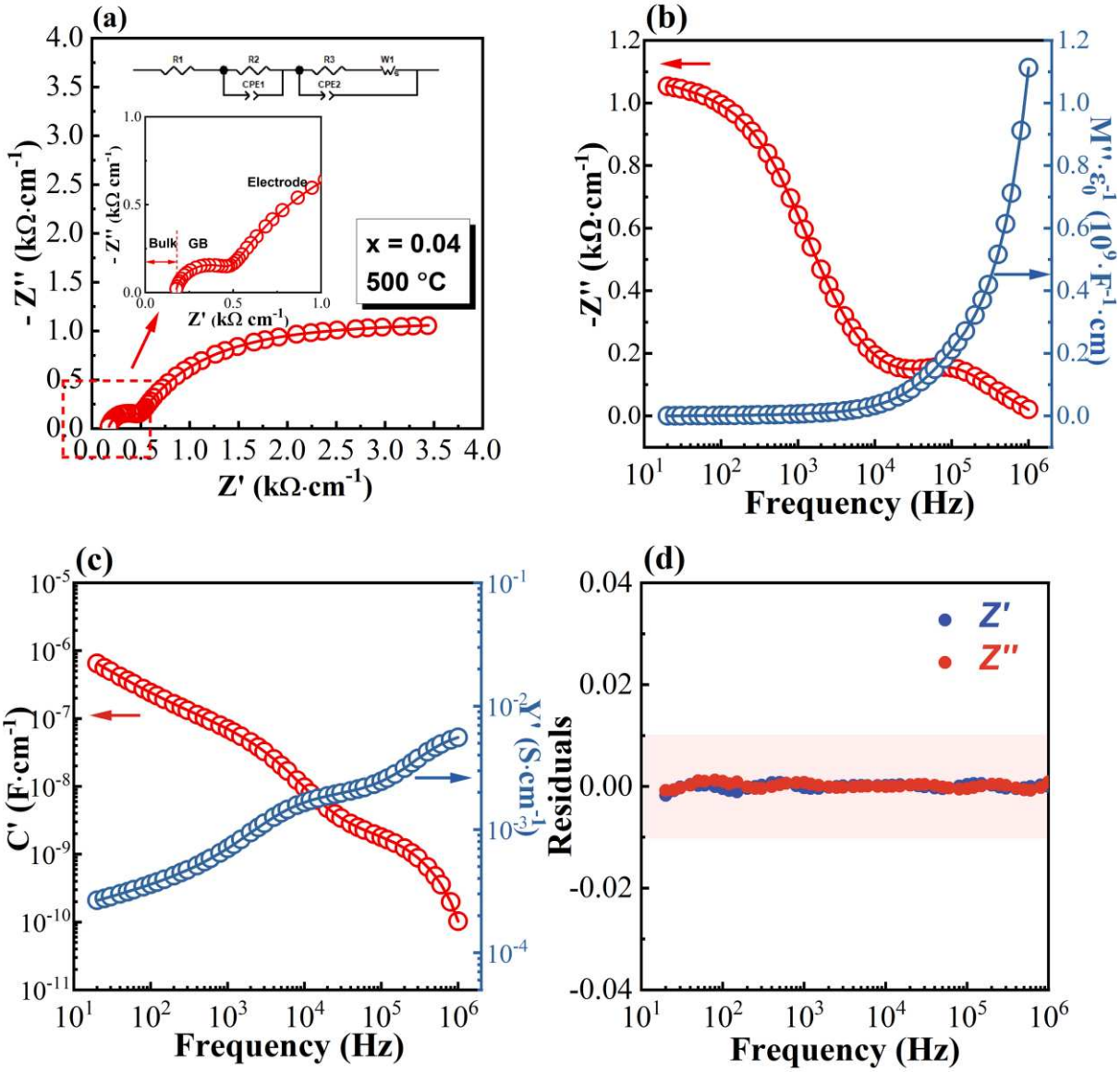

Figure 5. Impedance spectroscopy data and equivalent circuit fitting results presented in different formats for a selected composition, x = 0.04, at 500 °C. (**a**) Z^* plot and the equivalent circuit used for fitting; (**b**) $-Z''$-log$f$ and M''-log$f$ plots; (**c**) C'-log$f$ and Y'-log$f$ plots; (**d**) impedance residuals showing the quality of fit. In (**a**–**c**), open circles are experimental data and solid lines across the symbols are the fitting curve. The inset figure in (**a**) is the expanded view of the high-frequency region, as indicated by the dashed rectangle.

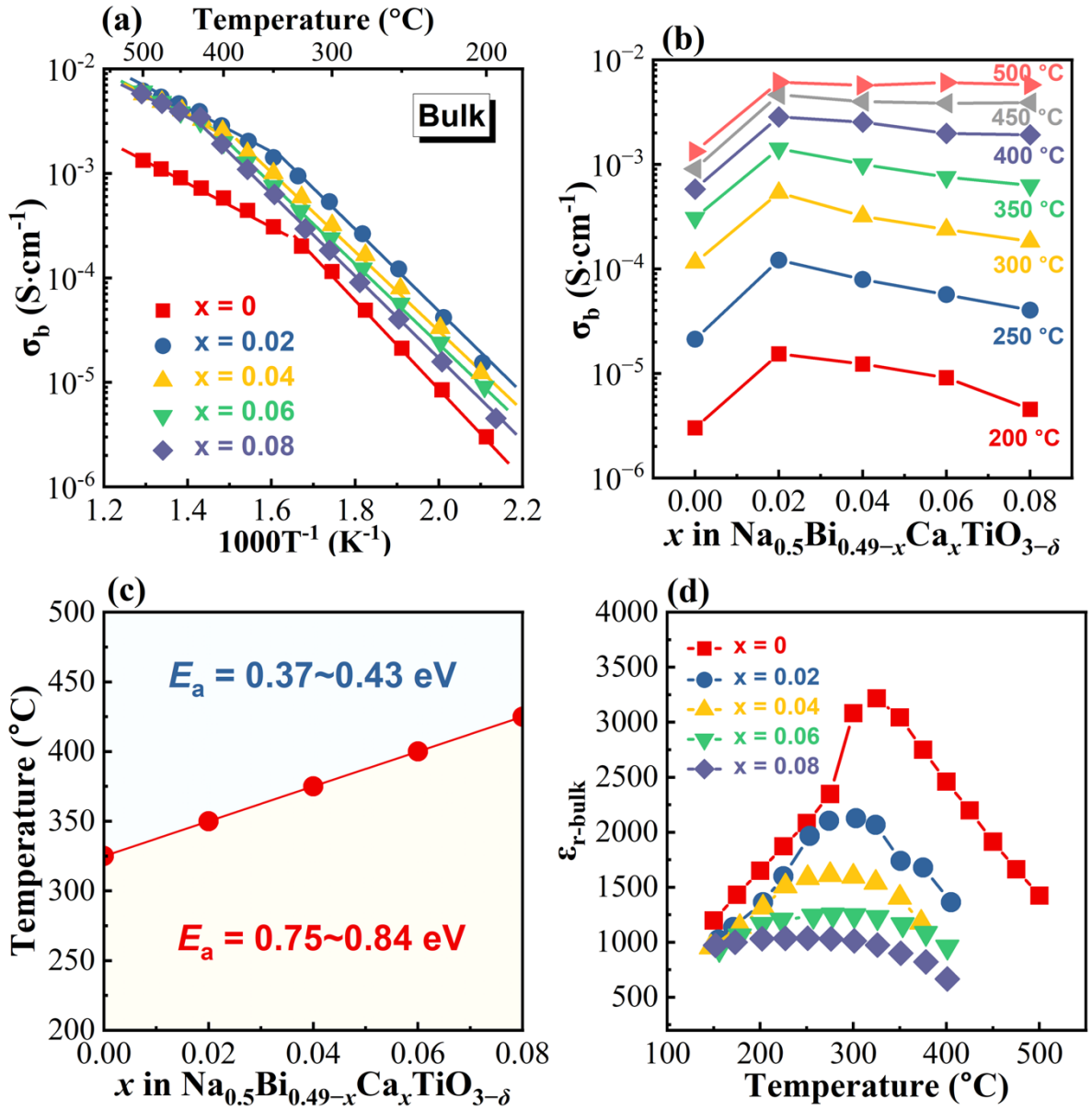

Figure 6. (**a**) Arrhenius plots for σ_b; (**b**) compositional dependence of σ_b at selected temperatures; (**c**) variation of T_{Ea} with x. E_a values in the temperature ranges 200 °C $\leq T \leq T_{Ea}$ and $T_{Ea} < T \leq 500$ °C, are also indicated in the figure. (**d**) $\varepsilon_{r\text{-bulk}}$ calculated from the bulk response as a function of temperature.

On the other hand, capacitance of the high-frequency bulk response can be calculated from equivalent circuit-fitting parameters according to $C = R^{(1-n)/n}Q^{1/n}$ [35], and then converted to the bulk permittivity $\varepsilon_{r\text{-bulk}}$ according to $\varepsilon_{r\text{-bulk}} = C/\varepsilon_0$, where ε_0 is the vacuum permittivity (8.85×10^{-14} F·cm^{-1}). The $\varepsilon_{r\text{-bulk}}$ of $Na_{0.5}Bi_{0.49-x}Ca_xTiO_{3-\delta}$ ceramics was plotted as a function of temperature and presented in Figure 6d. The $\varepsilon_{r\text{-bulk}}$ of the undoped $NB_{0.49}T$ had a strong dependence on temperature and showed a maximum ~3200 at 325 °C. Ca doping had a significant impact on the $\varepsilon_{r\text{-bulk}}$–$T$ profile: (1) $\varepsilon_{r\text{-bulk}}$ decreased with increasing Ca^{2+} doping level, which can be related to the lower polarizability of Ca^{2+} than Bi^{3+} (3.16 Å^3 versus 6.12 Å^3 [36]). This gives additional evidence that Ca^{2+} was successfully incorporated into $NB_{0.49}T$. (2) With increasing Ca^{2+}-doping level, $\varepsilon_{r\text{-bulk}}$ became less dependent on temperature, i.e., an almost temperature-independent ε_r between 150 and 350 °C could be observed for $x = 0.08$.

As the 2% Ca-doped $NB_{0.49}T$ exhibited the highest σ_b, impedance measurements over a wider frequency range (0.1 Hz to 1 MHz) were carried out for this composition in flowing nitrogen, air, and oxygen at various temperatures. As shown in Figure 7a, the Z^* plot at 400 °C was dominated by the large electrode response at low frequencies, which showed a weak dependence on the atmosphere. The bulk and GB responses at high- and intermediate-frequency ranges did not change with oxygen partial pressure (pO_2), as shown by the inset figure. The pO_2-independent σ_b (Figure 7b) suggests the electrical conduction was predominately ionic over the limited temperature and pO_2 range investigated.

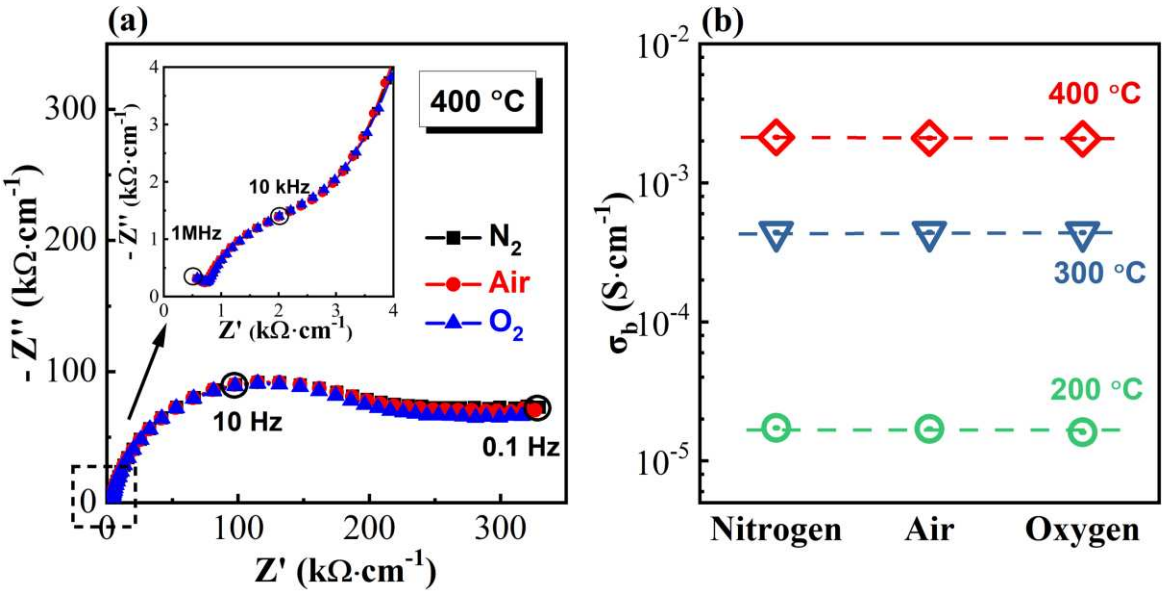

Figure 7. (**a**) Z^* plots for a selected composition, $x = 0.02$, measured in flowing N_2, air, and O_2 at 400 °C. The inset figure is an expanded view of the high-frequency region. (**b**) Bulk conductivity extracted from impedance data at different temperatures and atmospheres.

3.3. Dielectric Properties

The permittivity temperature (ε_r-T) profiles of $Na_{0.5}Bi_{0.49-x}Ca_xTiO_{3-\delta}$ ceramics measured at 1 MHz are presented in Figure 8a. At temperatures < 400 °C, the permittivity maximum decreased with increasing x, and ε_r was less dependent on temperature when the doping level was high (e.g., $x = 0.08$). This is consistent with that observed from the $\varepsilon_{r\text{-bulk}}$–$T$ relationship in Figure 7d. At temperatures > 400 °C, ε_r of the Ca-doped $NB_{0.49}T$ showed a further increase with increasing temperature until ~500 °C, which may be related to the GB or electrode effect and will be discussed later. A further increase in the temperature (T > 500 °C) caused a rapid drop of ε_r, which was caused by the non-negligible effect from induction when the conductivity of the measured ceramic was sufficiently high. As shown in Figure 8b, the dielectric loss (tan δ) of undoped $NB_{0.49}T$ showed a rapid increase with increasing temperature, and exceeded 0.4 at ~400 °C, which is a characteristic for oxide-ion-conducting NBT. In comparison, tan δ of Ca-doped $NB_{0.49}T$ ceramics showed a steeper increase with increasing temperature and exceeded 0.4 at ~300 °C due to the higher conductivity caused by Ca doping.

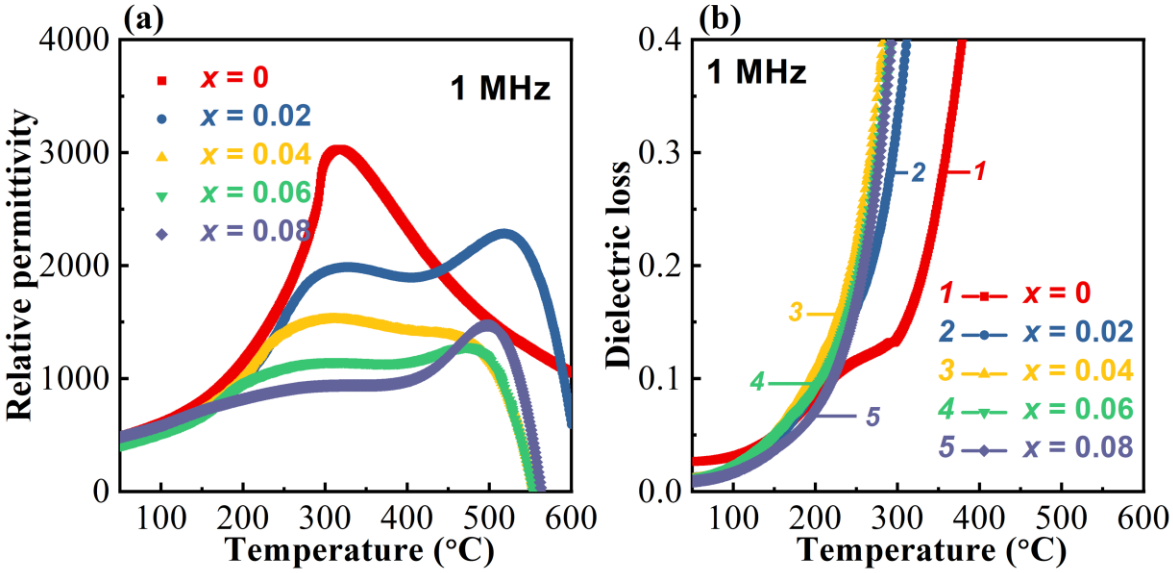

Figure 8. Dielectric spectroscopy of $Na_{0.5}Bi_{0.49-x}Ca_xTiO_{3-\delta}$: (**a**) relative permittivity at 1 MHz versus temperature; (**b**) dielectric loss at 1 MHz versus temperature.

4. Discussion

The major findings of this work are: (1) σ_b of $NB_{0.49}T$ can be enhanced by replacing Bi^{3+} by Ca^{2+}. The highest σ_b is reached in 2% Ca-doped $NB_{0.49}T$. Further increases in the doping level (x) decreases σ_b; (2) similar to $NB_{0.49}T$, σ_b–T^{-1} relationship of Ca-doped $NB_{0.49}T$ also shows a change in E_a from ~0.80 eV at lower temperatures to ~0.40 eV at high temperatures. The temperature at which E_a changes, T_{Ea}, depends on the doping level. The higher x, the higher T_{Ea}.

In $NB_{0.49}T$, oxygen vacancies are generated according to the following Kroger–Vink equation:

$$2Bi_{Bi}^{x} + 3O_{O}^{x} \overset{-Bi_2O_3}{\rightarrow} 2V_{Bi}^{'''} + 3V_{\ddot{O}} \quad (1)$$

When Bi^{3+} is partially replaced by Ca^{2+} doping, additional oxygen vacancies are created according to

$$2CaO \overset{Bi_2O_3}{\rightarrow} 2Ca_{Bi}^{'} + V_{\ddot{O}} + 2O_{O}^{x} \quad (2)$$

Occurrence of the reaction described by Equation (2) has been confirmed by the significant and systematic reduction of the maximum permittivity ($\varepsilon_{r\text{-}max}$) of $NB_{0.49}T$ with increasing Ca-doping level (Figures 6d and 8a). Moreover, the analyzed composition from EDS is close to the nominal composition (Figure 3), which also supports the successful incorporation of Ca^{2+} into $NB_{0.49}T$. As a consequence, the oxygen vacancy concentration, $[V_{\ddot{O}}]$ increases with increasing Ca-doping level x (Table 2). As conductivity is determined by the charge carrier concentration (n), charge (q), and mobility (μ) according to $\sigma = n{\cdot}q{\cdot}\mu$, the observed σ_b–x relationship suggests the mobility of oxygen ions as playing a dominant role for σ_b in Ca-$NB_{0.49}T$. Possible factors that influence the oxide ion mobility in Ca-doped $NB_{0.49}T$ are discussed, as follows:

(1) The average structure. Oxide ion conductivity in a perovskite lattice can usually be predicted empirically by the tolerance factor, t [37]; the lattice free volume, V_{sf} [27]; and the critical radius, r_C [38]. Equations for calculating the above three parameters can be found in our previous publications [7,39,40], and the values for Ca-doped $NB_{0.49}T$ are listed in Table 2. With increasing doping level, t decreases towards the optimum value of 0.96 [27]; furthermore, V_{sf} and r_C both increase, which are beneficial to the oxygen ion conduction in perovskites. This fails to explain the σ_b–x relationship in Figure 6b.

(2) The local structure. Previous studies by first principles calculations have revealed the significant impact of the local structure on oxygen ion diffusion in NBT [22,41]. In perovskites, oxygen ion migration occurs through a saddle point, which is a triangle formed by two A-site cations and one B-site cation [42]. In NBT, the energy barriers for oxygen ion migration through the Na-Na-Ti, Na-Bi-Ti, and Bi-Bi-Ti saddle points are 1.0–1.3, 0.6–0.85 and 0.22 eV, respectively [22]. As high polarizability of Bi^{3+} and weak Bi–O bonds are critical to the high mobility of oxygen ions, replacement of Bi^{3+} by Ca^{2+} with a lower polarizability and a stronger bond with oxygen increases the energy barrier for oxygen migration, and therefore reduces the oxygen ion mobility.

(3) Trapping of oxygen vacancies by Ca'_{Bi}. Trapping of the positively charged oxygen vacancies by the negatively charged acceptor-type dopants has been widely observed in oxide ion conductors. Evidence comes from the "volcano"-shaped relationship between conductivity and doping level, and a decrease in the activation energy at higher temperatures when the defect associates are released [43]. In NBT, trapping between the B-site acceptor dopants and oxygen vacancies has been supported by first-principles calculations. Although the calculations suggest A-site acceptor dopants are beneficial to oxygen ion diffusion, experimental results on Li- and K-doped NBT still show a drop in the σ_b when the doping level exceeds 4% [18]. Trapping of oxygen vacancies by Ca'_{Bi} can be another possible reason for the reduced oxygen ion mobility.

Table 2. Oxygen deficiency, oxygen vacancy concentration, and average structural parameters of $Na_{0.5}Bi_{0.49-x}Ca_xTiO_{3-\delta}$ ($0 \leq x \leq 0.08$) ceramics.

x	δ	$[V_{\ddot{O}}]$ (%)	t	V_{sf}	r_C (Å)
0	0.015	0.5	0.9792	0.1949	0.9071
0.02	0.025	0.83	0.9789	0.1969	0.9074
0.04	0.035	1.17	0.9785	0.1988	0.9076
0.06	0.045	1.5	0.9781	0.2008	0.9079
0.08	0.055	1.83	0.9778	0.2027	0.9082

The change of E_a for σ_b at ~300 °C is characteristic of oxide-ion-conducting NBT. The temperature at which E_a changes is associated with a maximum in the permittivity–temperature profile. Several possible reasons for a change of E_a, including the coexistence of rhombohedral and tetragonal phases at 250–400 °C [6], and dissociation of defect clusters and/or changing of conduction paths associated with the various NBT polymorphs [14,23] have been proposed. The reason why Ca doping can delay the change of E_a may be related to the phase transition behavior of $Na_{0.5}Bi_{0.49-x}Ca_xTiO_{3-\delta}$. $CaTiO_3$ has an orthorhombic structure. Previous studies [25,26] have shown the coexistence of rhombohedral and orthorhombic phases at room temperature and coexistence of orthorhombic and tetragonal phases at 200–450 °C for the solid solution $(NBT)_{0.9}(CaTiO_3)_{0.1}$. Although here the doping level is smaller than 10%, and Ca^{2+} only nominally substitutes Bi^{3+} (instead of both Na^+ and Bi^{3+}), it is still possible that Ca doping influences the phase transition behavior. However, further in-depth structural analysis is required to understand the relationship between phase transition and the σ_b–T^{-1} relationship.

5. Conclusions

$Na_{0.5}Bi_{0.49-x}Ca_xTiO_{3-\delta}$ ($0 \leq x \leq 0.08$) ceramics were prepared by solid-state reaction, and their electrical and dielectric properties were investigated primarily by impedance spectroscopy. The major conclusions are summarized as follows:

Replacement of Bi^{3+} by Ca^{2+} on the A-site of $NB_{0.49}T$ is an effective approach for enhancing the σ_b of $NB_{0.49}T$ by creating oxygen vacancies. The highest σ_b (0.006 $S{\cdot}cm^{-1}$) is achieved by 2% Ca^{2+} doping. Further increase in the doping level decreases σ_b, which is more pronounced at temperatures below ~350 °C. The σ_b–x relationship can be attributed

to the reduced cell volume caused by Ca^{2+} doping, and the defect association between Ca'_{Bi} and $V^{\cdot\cdot}$.

Similar to undoped $NB_{0.49}T$, Ca-doped $NB_{0.49}T$ ceramics show a change in the activation energy for bulk conduction from ~0.80 eV at low temperatures to ~0.40 eV at high temperatures. However, Ca doping can increase the temperature of the activation energy for bulk conduction. This may be related to the delay in phase transition caused by Ca doping, which has been observed in NBT-$CaTiO_3$ solid solutions. Further in-depth investigations of the crystal structure and its evolution with temperature are in progress to support the above speculation.

Ca doping can reduce the temperature dependence of permittivity of $NB_{0.49}T$. This provides a strategy for obtaining a stable permittivity in certain temperature ranges for NBT-based material by Ca incorporation; however, in this case an insulating NBT and a different doping strategy should be considered to reduce the dielectric loss.

Author Contributions: Conceptualization, F.Y. and D.C.S.; methodology, F.Y. and P.W.; software, F.Y.; validation, F.Y., Q.H. and D.C.S.; formal analysis, F.Y.; investigation, F.Y., Y.H. and P.W.; resources, F.Y., Q.H. and D.C.S.; data curation, F.Y., Y.H. and P.W.; writing—original draft preparation, F.Y.; writing—review and editing, F.Y., Q.H. and D.C.S.; visualization, F.Y.; supervision, F.Y., Q.H. and D.C.S.; project administration, F.Y., Q.H. and D.C.S.; funding acquisition, F.Y., Q.H. and D.C.S. All authors have read and agreed to the published version of the manuscript.

Funding: This research was funded by [National Natural Science Foundation of China] grant number [52072239], [52234010], and [EPSRC] grant number [EP/L027348/1].

Conflicts of Interest: The authors declare no conflict of interest.

References

1. Li, M.; Pietrowski, M.J.; de Souza, R.A.; Zhang, H.; Reaney, I.M.; Cook, S.N.; Kilner, J.A.; Sinclair, D.C. A family of oxide-ion conductors based on the ferroelectric perovskite $Na_{0.5}Bi_{0.5}TiO_3$. *Nat. Mater.* **2014**, *13*, 31–35. [CrossRef] [PubMed]
2. Li, M.; Zhang, H.; Cook, S.N.; Li, L.; Kilner, J.A.; Reaney, I.M.; Sinclair, D.C. Dramatic influence of A-site nonstoichiometry on the electrical conductivity and conduction mechanisms in the perovskite oxide $Na_{0.5}Bi_{0.5}TiO_3$. *Chem. Mater.* **2015**, *27*, 629–634. [CrossRef]
3. Chen, X.; Zeng, J.; Yan, X.; Zhou, M.; Tang, P.; Liang, T.; Li, W. Effects of Bi deficiency on the microstructural and conductive properties of $Na_{0.5}Bi_{0.5}TiO_3$ (NBT) perovskite. *Solid State Ion.* **2017**, *209*, 152–162. [CrossRef]
4. Chen, X.; Zhou, M.; Shi, J.; Liang, T.; Zeng, J.; Yan, X.; Luo, N.; Li, W.; Wei, Y. Microstructure and electrical conductivity of A-site fully stoichiometric $Na_{0.5+x}Bi_{0.5-x}TiO_{3-\delta}$ with different Na/Bi ratios. *Ceram. Int.* **2019**, *45*, 11438–11447. [CrossRef]
5. Shi, J.; Liu, X.; Zhu, F.; Tian, W.; Xia, Y.; Li, T.; Rao, R.; Zhang, T.; Liu, L. Oxygen vacancy migration and its lattice structural origin in A-site non-stoichiometric bismuth sodium titanate perovskites. *J. Mater.* **2022**, *8*, 719–729. [CrossRef]
6. Yang, F.; Zhang, H.; Li, L.; Reaney, I.M.; Sinclair, D.C. High ionic conductivity with low degradation in A-site strontium-doped nonstoichiometric sodium bismuth titanate perovskite. *Chem. Mater.* **2016**, *28*, 5269–5273. [CrossRef]
7. Yang, F.; Wu, P.; Sinclair, D.C. Enhanced bulk conductivity of A-site divalent acceptor-doped non-stoichiometric sodium bismuth titanate. *Solid State Ion.* **2017**, *299*, 38–45. [CrossRef]
8. Yang, F.; Li, M.; Li, L.; Wu, P.; Pradal-Velázquez, E.; Sinclair, D.C. Optimisation of oxide-ion conductivity in acceptor-doped $Na_{0.5}Bi_{0.5}TiO_3$ perovskite: Approaching the limit? *J. Mater. Chem. A* **2017**, *5*, 21658–21662. [CrossRef]
9. Bhattacharyya, R.; Omar, S. Electrical conductivity study of B-site Ga doped non-stoichiometric sodium bismuth titanate ceramics. *J. Alloy. Compd.* **2018**, *746*, 54–61. [CrossRef]
10. Li, M.Y.; He, C.; Wang, W.G.; Hao, G.L.; Li, X.Y.; Liu, T.; Wang, X.F.; Wang, D. Investigation of Ga doping for non-stoichiometric sodium bismuth titanate ceramics. *J. Mater. Sci. Mater. Electron.* **2021**, *32*, 16104–16112. [CrossRef]
11. Singh, P.; Pandey, R.; Singh, P. Polyol-mediated synthesis of Bi-deficient Mg^{2+}-doped sodium bismuth titanate and study of oxide ion migration behavior with functional properties. *J. Alloy. Compd.* **2021**, *860*, 158492. [CrossRef]
12. Bhattacharyya, R.; Das, S.; Omar, S. High ionic conductivity of Mg^{2+}-doped non-stoichiometric sodium bismuth titanate. *Acta Mater.* **2018**, *159*, 8–15. [CrossRef]
13. Lu, Y.; López, C.A.; Wang, J.; Alonso, J.A.; Sun, C. Insight into the structure and functional application of Mg-doped $Na_{0.5}Bi_{0.5}TiO_3$ electrolyte for solid oxide fuel cells. *J. Alloy. Compd.* **2018**, *752*, 213–219. [CrossRef]
14. Koch, L.; Steiner, S.; Meyer, K.; Seo, I.; Albe, K.; Frömling, T. Ionic conductivity of acceptor doped sodium bismuth titanate: Influence of dopants, phase transitions and defect associates. *J. Mater. Chem. C* **2017**, *5*, 8958–8965. [CrossRef]
15. Steiner, S.; Seo, I.; Ren, P.; Li, M.; Keeble, D.J.; Frömling, T. The effect of Fe-acceptor doping on the electrical properties of $Na_{1/2}Bi_{1/2}TiO_3$ and $0.94(Na_{1/2}Bi_{1/2})TiO_3$-$0.06BaTiO_3$. *J. Am. Ceram. Soc.* **2019**, *102*, 5295–5304. [CrossRef]

16. Groszewicz, P.B.; Koch, L.; Steiner, S.; Ayrikyan, A.; Webber, K.G.; Frömling, T.; Albe, K.; Buntkowsky, G. The fate of aluminium in (Na,Bi)TiO_3-based ionic conductors. *J. Mater. Chem. A* **2020**, *8*, 18188–18197. [CrossRef]
17. Shih, D.P.C.; Aguadero, A.; Skinner, S.J. Improvement of ionic conductivity in A-site lithium doped sodium bismuth titanate. *Solid State Ion.* **2018**, *317*, 32–38. [CrossRef]
18. Shih, D.P.C.; Aguadero, A.; Skinner, S.J. A-site acceptor-doping strategy to enhance oxygen transport in sodium-bismuth-titanate perovskite. *J. Am. Ceram. Soc.* **2023**, *106*, 100–108. [CrossRef]
19. Liu, X.; Zhao, Y.; Hu, H.; Du, H.; Shi, J. Ionic conductive and dielectric properties of samarium isovalent doping in non-stoichiometric bismuth sodium titanate perovskite. *Ionics* **2019**, *25*, 2729–2734. [CrossRef]
20. Shi, J.; Rao, R.; Tian, W.; Xu, X.; Liu, X. Anomalous electrical performance of A-site double-bivalent-doped $Bi_{0.49}Na_{0.5}TiO_{3-\delta}$ ceramics from nominal oxygen deficiency to excess. *Ceram. Int.* **2022**, *48*, 5210–5216. [CrossRef]
21. Liu, X.; Du, H.; Shi, J.; Hu, H.; Hao, X. Ionic conduction and anomalous diffusion in Sr and Ga acceptor co-doped bismuth sodium titanate solid solutions. *ECS J. Solid State Sci. Technol.* **2018**, *7*, N96–N100. [CrossRef]
22. He, X.; Mo, Y. Accelerated materials design of $Na_{0.5}Bi_{0.5}TiO_3$ oxygen ionic conductors based on first principles calculations. *Phys. Chem. Chem. Phys.* **2015**, *17*, 18035–18044. [CrossRef] [PubMed]
23. Meyer, K.; Albe, K. Influence of phase transitions and defect associates on the oxygen migration in the ion conductor $Na_{1/2}Bi_{1/2}TiO_3$. *J. Mater. Chem. A* **2017**, *5*, 4368–4375. [CrossRef]
24. Koch, L.; Steiner, S.; Hoang, A.; Klomp, A.J.; Albe, K.; Frömling, T. Revealing the impact of acceptor dopant type on the electrical conductivity of sodium bismuth titanate. *Acta Mater.* **2022**, *229*, 117808. [CrossRef]
25. Ranjan, R.; Garg, R.; Kothai, V.; Agrawal, A.; Senyshyn, A.; Boysen, H. Phases in the $(1-x)Na_{0.5}Bi_{0.5}TiO_3$-$(x)CaTiO_3$ system. *J. Phys. Condens. Matter* **2010**, *22*, 075901. [CrossRef]
26. Roukos, R.; Zaiter, N.; Chaumont, D. Relaxor behaviour and phase transition of perovskite ferroelectrics-type complex oxides $(1-x)Na_{0.5}Bi_{0.5}TiO_3-xCaTiO_3$ system. *J. Adv. Ceram.* **2018**, *7*, 124–142. [CrossRef]
27. Hayashi, H.; Inaba, H.; Matsuyama, M.; Lan, N.G.; Mokiya, M.; Tagawa, H. Structural consideration on the ionic conductivity of perovskite-type oxides. *Solid State Ion.* **1999**, *122*, 1–15. [CrossRef]
28. Larson, A.C.; Von Drelle, R.B. *General Structure Analysis System (GSAS)*; Los Alamos National Laboratory Report LAUR 86-748 (2004); Los Alamos National Laboratory: Los Alamos, NM, USA, 2004.
29. Toby, B.H. EXPGUI, a graphical user interface for GSAS. *J. Appl. Crystallogr.* **2001**, *34*, 210–213. [CrossRef]
30. Shannon, R.D. Revised effective ionic radii and systematic studies of interatomic distances in halides and chalcogenides. *Acta Crystallogr. Sect. A* **1976**, *31*, 751–767. [CrossRef]
31. Jones, G.O.; Thomas, P.A. Investigation of the structure and phase transitions in the novel A-site substituted distorted perovskite compound $Na_{0.5}Bi_{0.5}TiO_3$. *Acta Crystallogr. Sect. B* **2002**, *58*, 168–178. [CrossRef]
32. Irvine, J.T.S.; Sinclair, D.C.; West, A.R. Electroceramics: Characterization by impedance spectroscopy. *Adv. Mater.* **1990**, *2*, 132–138. [CrossRef]
33. Masó, N.; West, A.R. Electronic conductivity in yttria-stabilized zirconia under a small dc bias. *Chem. Mater.* **2015**, *27*, 1552–1558. [CrossRef]
34. MacDonald, J.R. *Impedance Spectroscopy—Emphasizing Solid Materials and Systems*; Wiley: New York, NY, USA, 1987.
35. Fleig, J. The grain boundary impedance of random microstructures: Numerical simulations and implications for the analysis of experimental data. *Solid State Ion.* **2002**, *150*, 181–193. [CrossRef]
36. Grimes, N.W.; Grimes, R.W. Dielectric polarizability of ions and the corresponding effective number of electrons. *J. Phys. Condens. Matter* **1998**, *10*, 3029–3034. [CrossRef]
37. Beskow, G. V. M. Goldschmidt: Geochemische Verteilungsgesetze der Elemente. *Geol. Fören. I Stockh. Förh.* **1924**, *46*, 738–743. [CrossRef]
38. Kilner, J.A.; Brook, R.J. A study of oxygen ion conductivity in doped non-stoichiometric oxides. *Solid State Ion.* **1982**, *6*, 237–252. [CrossRef]
39. Yang, F.; Wu, P.; Sinclair, D.C. Suppression of electrical conductivity and switching of conduction mechanisms in 'stoichiometric' $(Na_{0.5}Bi_{0.5}TiO_3)_{1-x}(BiAlO_3)_x$ $(0 \leq x \leq 0.08)$ solid solutions. *J. Mater. Chem. C* **2017**, *5*, 7243–7252. [CrossRef]
40. Yang, F.; Wu, P.; Sinclair, D.C. Electrical conductivity and conduction mechanism in $(Na_{0.5}Bi_{0.5}TiO_3)_{1-x}(BiScO_3)_x$ $(0.00 \leq x \leq 0.35)$ solid solutions. *J. Mater. Chem. C* **2018**, *6*, 11598–11607. [CrossRef]
41. Dawson, J.A.; Chen, H.; Tanaka, I. Crystal structure, defect chemistry and oxygen ion transport of the ferroelectric perovskite, $Na_{0.5}Bi_{0.5}TiO_3$: Insights from the first principles calculations. *J. Mater. Chem. A* **2015**, *3*, 16574–16582. [CrossRef]
42. Islam, M.S. Ionic transport in ABO_3 perovskite oxides: A computer modelling tour. *J. Mater. Chem.* **2000**, *10*, 1027–1038. [CrossRef]
43. Arachi, Y.; Sakai, H.; Yamamoto, O.; Takeda, Y.; Imanishai, N. Electrical conductivity of the ZrO_2-Ln_2O_3 (Ln = lanthanides) system. *Solid State Ionics* **1999**, *121*, 133–139. [CrossRef]